THE JOURNAL OF PHYSICAL CHEMISTRY C
A JOURNAL OF THE AMERICAN CHEMICAL SOCIETY

pubs.acs.org/JPCC

Article

K-Edge XANES Investigation of Fe-Based Oxides by Density Functional Theory Calculations

Jing Zhu, Zhenhua Zeng,* and Wei-Xue Li*

Cite This: *J. Phys. Chem. C* 2021, 125, 26229–26239

Read Online

ABSTRACT: X-ray absorption spectroscopy (XAS) is a powerful technique for simultaneously characterizing the oxidation states and local structures of working catalysts and battery materials, among others. However, deciphering the apparent oxidation state through XAS remains challenging because of the high sensitivity of spectra to multiple factors. Here, comprehensive first-principles calculations of X-ray absorption near-edge structure (XANES) spectra of a series of Fe-based catalysts and battery electrodes, including FeO, Fe_2O_3, $Fe(OH)_2$, FeOOH, $FeAl_2O_4$, and $MFeO_2$ (M = Li, Na, or K), were performed to shed light on the issue by dissecting the dependence of XANES line shapes on detailed electronic and geometric structures. We revealed that, in comparison with the composition and factors usually extracted from XAS measurements (i.e., the oxidation state and local structure), nonlocal structures (e.g., crystal structure) that cannot be straightforwardly obtained from XAS experiments are more dominant factors of the XANES line shapes of the main edge, main peak, and postedge. As demonstrated through Fe compounds with the same or similar nonlocal structures, their line shapes are alike and shift in response to a change in the chemical environment. On the other hand, we found that the local coordination (octahedra vs tetrahedra) and the oxidation state are more dominant on the intensity of the pre-edge and the energy splitting between the pre-edge and the main edge, respectively. We demonstrated that clarifying these control factors and origins not only provides valuable insights into reliable assignment of spectra and understanding semiempirical rules but also unravels the structural information that is not directly accessible in XAS measurements.

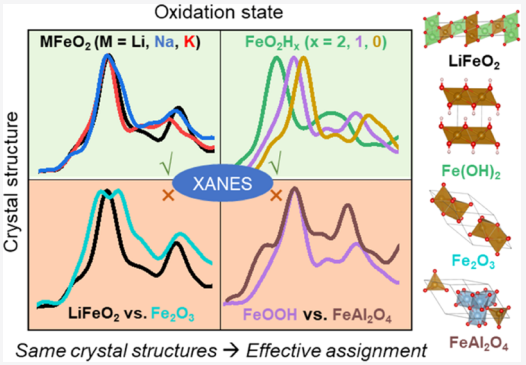

INTRODUCTION

Establishing rigorous structure–property relationships lies at the heart of catalysis and battery research, in which the characterization of geometric structures and electronic structures of catalytically active phases is usually a prerequisite. For this purpose, a variety of spectroscopic and scattering techniques have been developed, such as ultraviolet photoelectron spectroscopy, X-ray photoelectron spectroscopy, X-ray absorption and emission spectroscopy, small- and wide-angle X-ray scattering, and resonant inelastic X-ray scattering.[1−7] Among them, X-ray absorption spectroscopy (XAS) has unique advantages over others to probe catalysts at work.[8−15] Specifically, it simultaneously provides element-specific electronic structures (e.g., the oxidation state) and geometric structures of a broad range of catalysts under a variety of experimental conditions through X-ray absorption near-edge spectroscopy (XANES) and the extended X-ray absorption fine structure (EXAFS), respectively.[8] Under operando conditions, it can provide key information of the active phases under realistic reaction conditions, including electrocatalytic reactions at electrified liquid–solid interfaces, which render them inadequate for those techniques designed for experiments in vacuum or at gas–solid interfaces.[16] For XANES, because of the electronic structure nature, it is highly sensitive to not only the oxidation state but also local coordination, bond length, chemical composition, and crystal structure,[8,17−19] among others, which in turn alter the electronic structure and corresponding spectra. Such a high sensitivity endows XANES with an element-specific fingerprint of catalysts for a variety of applications. Thus, operando XAS has been widely used to simultaneously characterize the complex geometric structure and oxidation state of novel electrocatalysts.[20−27]

While extracting the local geometry from EXAFS is relatively straightforward, deciphering the oxidation state from the XANES spectra is highly complex because of their high sensitivity to a variety of factors, as mentioned above.[18] For decades, the main edges of measured XANES spectra and associated oxidation states have been interpreted by referring to standard samples with well-defined crystal structures and compositions.[8] For example, for Fe XANES spectra, Fe^0 in

Received: September 26, 2021
Revised: November 2, 2021
Published: November 18, 2021

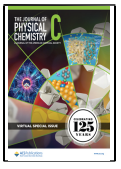

https://doi.org/10.1021/acs.jpcc.1c08461
J. Phys. Chem. C 2021, 125, 26229–26239

metallic Fe, Fe^{2+} in FeO or $Fe(OH)_2$, and Fe^{3+} in Fe_2O_3 or FeOOH are usually used as standard references.[23,24,26−29] However, the fingerprint feature of XANES, dictated by unique electronic structures for an element in each compound, suggests that the main edge of another compound might not be straightforwardly derived based on the spectra of those standard references. Indeed, for Fe^{2+} and Fe^{3+} as examples, it has been demonstrated through a large number of well-defined catalysts and minerals that most of them, even those with the same local structures but different crystal structures and/or compositions, have little or no resemblance to that of FeO or Fe_2O_3 on the main edge.[30,31] For newly developed catalysts with unclear compositions and/or nonlocal structures under realistic reaction conditions, their oxidation states might not be extracted reliably by comparing the main edge of measured XANES spectra with that of FeO or Fe_2O_3. This prevents a fundamental understanding of the structure−property relationship and rational design of new catalysts. Interpreting Fe oxidation states on the basis of pre-edges is also highly challenging, though it also has been extensively studied.[8,30,32,33] Due to the low intensity and the complex shapes, it is not always easy to separate the weak pre-edge from the main edge, resulting in a large uncertainty when determining the energy positions and consequently the energy shifts.[18,30,32] While the factors that influence the discernibility of pre-edge have been extensively studied, the fundamental origin is still unclear.

An accurate oxidation state may be better derived through the following two strategies. The first one is to enlarge the space of reference samples. However, measuring an element in a variety of compounds experimentally remains too expensive and time-consuming. With the advancements of simulation methods and codes,[34−40] it becomes possible to do so through first-principles calculations, such as developing a computational database on density functional theory (DFT) calculations of XANES spectra.[13,41] However, the exhaustive search in materials space to exactly match the line shape of XANES is still not an efficient way, considering unavoidable uncertainties in XANES modeling and consequent discrepancies between measured and calculated XANES spectra.[41−45] It is especially challenging for the newly developed catalysts with unique compositions and complex geometric structures, for which both the as-prepared phases and the active phases under operando conditions are likely not within the existing materials' space.[4,20]

The second strategy is to decipher the oxidation state based on a fundamental understanding of the dominant factors that govern the evolution of XANES line shapes. To achieve such a fundamental understanding, it is essential to conduct a rigorous study on the dependence of the XANES line shapes on multiple factors, such as the oxidation state, local coordination number, chemical composition, and nonlocal geometry (crystal structure). While it is challenging to do a well-controlled comparison of all of these factors through experiments, it is feasible through first-principles calculations due to significant progress in XANES modeling.[21,34−39,46] However, the investigations to derive the dominant factor in XANES line shapes and fundamental origins are still lacking and remain a challenge of the assignment of oxidation states by the semiempirical rules, especially involving the high-valent metals (e.g., Fe^{4+}) in crystalline compounds. It is worth noting that, although obtaining the local geometry and the oxidation state is the primary purpose of XAS measurements, achieving such a fundamental understanding of the dependence on the crystal structure may significantly extend the power of this unique technique by unraveling the nonlocal structure hidden in the measured XANES spectrum.

Here, we resorted to first-principles calculations on Fe-based oxides with a wide range of oxidation states, local geometries, compositions, and crystal structures, allowing to dissect the complex XANES and underlying physics. We chose Fe-based oxides and Fe K-edge XANES mainly for two reasons. First, Fe-based oxides play a central role in various heterogeneous catalysts, electrocatalysts, and batteries.[21,27,28,47−49] Second, Fe K-edge XANES spectra are abundant in the literature for comparison,[30,31] though deciphering the corresponding oxidation state through XANES remains a challenge. In addition to the standard references of FeO, Fe_2O_3, $Fe(OH)_2$, and FeOOH with different oxidation states and compositions considered, FeO_2 with a higher oxidation state and $FeAl_2O_4$ and layered $MFeO_2$ (M = Li, Na, or K) with more involved compositions and structures were considered to reveal the role of nonlocal structures in XANES spectra. For this purpose, we also considered different crystal phases for FeO and $LiFeO_2$. We found that Fe K-edge XANES spectra are sensitive to the oxidation state, local coordination, chemical composition, and crystal structure due to the unique electronic structure of Fe in each individual compound. However, the nonlocal structure determined essentially by the crystal structure was revealed to dominate the Fe K-edge XANES line shapes, in particular the corresponding main edges and postedges. However, the intensity of the pre-edge and the energy splitting between the pre-edge and the main edge are more sensitive to the local coordination (octahedra vs tetrahedra) and the oxidation state, respectively. We demonstrated that clarifying these dependencies and underlying origins can not only provide insights into the reliable assignment of spectra but also unravel the critical nonlocal structures hidden in the measured spectra.

■ COMPUTATIONAL METHODS

Spin-polarized density functional theory (DFT) calculations were performed using the GPAW code[50−52] through the Python-based atomic simulation environment (ASE).[53] The PBE + U method (U_{Fe} = 2.5 eV) was employed to describe strongly correlated Fe oxides and hydroxides.[54,55] A grid spacing of 0.2 Å was used for the real-space representation of the smooth wave functions. A total energy and eigenstate convergence of 5×10^{-4} and 4×10^{-8} eV, respectively, were employed for the electronic self-consistent field loop. The equilibrium geometries are obtained when the maximum atomic forces are smaller than 0.01 eV/Å. Monkhorst−Pack k-point grids are used for Brillouin zone integration. For example, for the unit cell of FeO with rocksalt structure, we use a (5 × 5 × 5) grid. For the other (hydroxy)oxides, we use equivalent or denser k-point grids. The calculated lattice constants, along with the spin states and the corresponding Fe atomic magnetic moments, are summarized in Tables S1 and S2 in the Supporting Information The differences between the calculated and experimental lattice constants are generally within 2%, which is a common error bar for standard generalized gradient approximations (GGA) and GGA + U calculations.[56−59]

The Fe K-edge spectra were simulated using GPAW on the basis of the Haydock recursion method with the half-core-hole potential or the so-called transition potential.[60,61] The absolute energy scale was computed with the ΔSCF method, in which the excited states are optimized self-consistently with a full

https://doi.org/10.1021/acs.jpcc.1c08461
J. Phys. Chem. C 2021, 125, 26229−26239

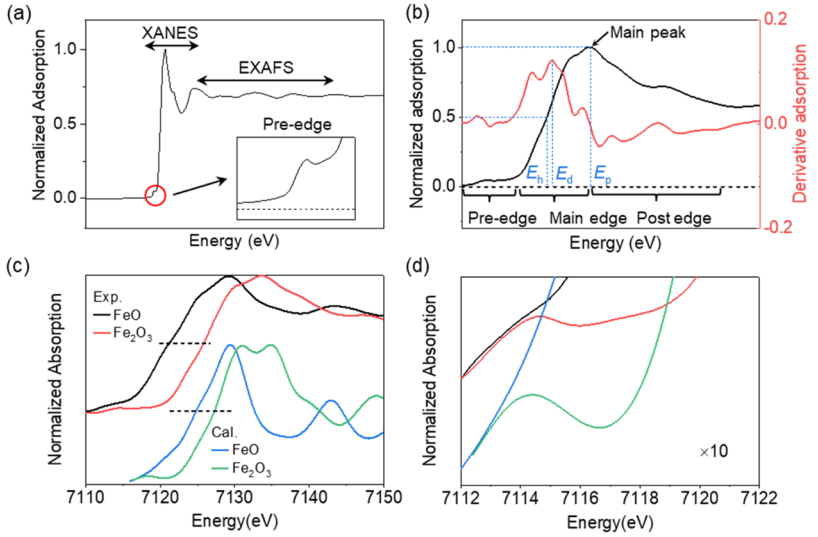

Figure 1. Schematic and dependence of XAS spectra on the oxidation state. (a) Schematic of XANES and EXFAS in XAS spectra. The inset shows the pre-edge of XANES spectra. (b) Schematic of XANES spectrum (black line) and the corresponding first-order derivative adsorption spectrum (red line), where the main peak position (E_p), the half-height of the main peak (E_h), and the maximum point in the derivative spectrum (E_d) are three common parameters that are used to compare the edge shift. (c) Simulated (denoted Cal.) Fe K-edge XANES spectra of Fe^{2+} and Fe^{3+} in FeO ($Fm\bar{3}m$) and Fe_2O_3 ($R\bar{3}c$). The measured XANES spectra (denoted Exp.) of FeO and α-Fe_2O_3 from our previous work are also given.[4] (d) Ten-time magnification of (c) to show the pre-edge feature. The dashed horizontal lines in (c) indicate the half-height of the main peak to easily distinguish the edge position E_h.

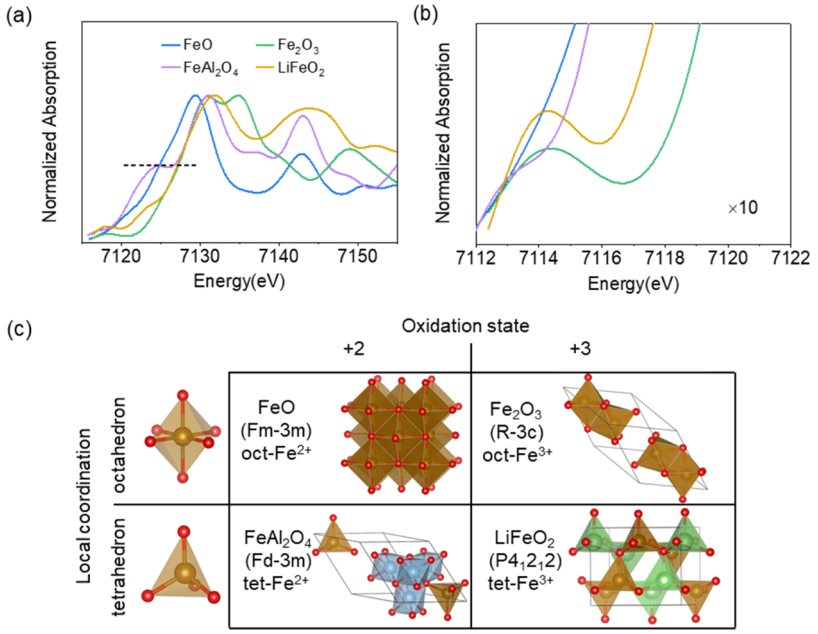

Figure 2. Dependence of XAS spectra on the oxidation state and the local coordination. (a) Simulated Fe K-edge XANES spectra of Fe^{2+} and Fe^{3+} in octahedron and tetrahedron coordinations, respectively. (b) Ten-time magnification of (a) to show the pre-edge feature. (c) Atomic structures of the oxides used in the simulation. Fe, O, Al, and Li atoms are in brown, red, blue, and green, respectively. The dashed horizontal lines in (a) indicate the half-height of the main peak to easily distinguish the edge position E_h.

core-hole in the 1s orbital and an extra electron added to the unoccupied state, and the total energy difference to the ground state gives the absolute energy with respect to the first unoccupied state. The first unoccupied state is represented by the Fermi level, which can be more reliably determined than the lowest unoccupied orbitals by the density functional theory for solids with fractional occupation. To facilitate the comparison, absorption coefficients were normalized by assuming the same intensity of white lines for all (hydroxy)-oxides. Unless otherwise stated, simulated XANES spectra were broadened with a parameter of 3 eV, which is equivalent to the full width at half-maximum (FWHM) in the experiment.

RESULTS AND DISCUSSION

Figure 1a shows the features of a typical X-ray absorption spectrum (XAS) from experimental measurements. Generally, it is divided into two regimes: X-ray absorption near-edge structure (XANES) and extended X-ray absorption fine structure (EXAFS). XANES is characterized by a weak pre-adsorption edge (pre-edge), and a rising main adsorption edge

https://doi.org/10.1021/acs.jpcc.1c08461
J. Phys. Chem. C 2021, 125, 26229−26239

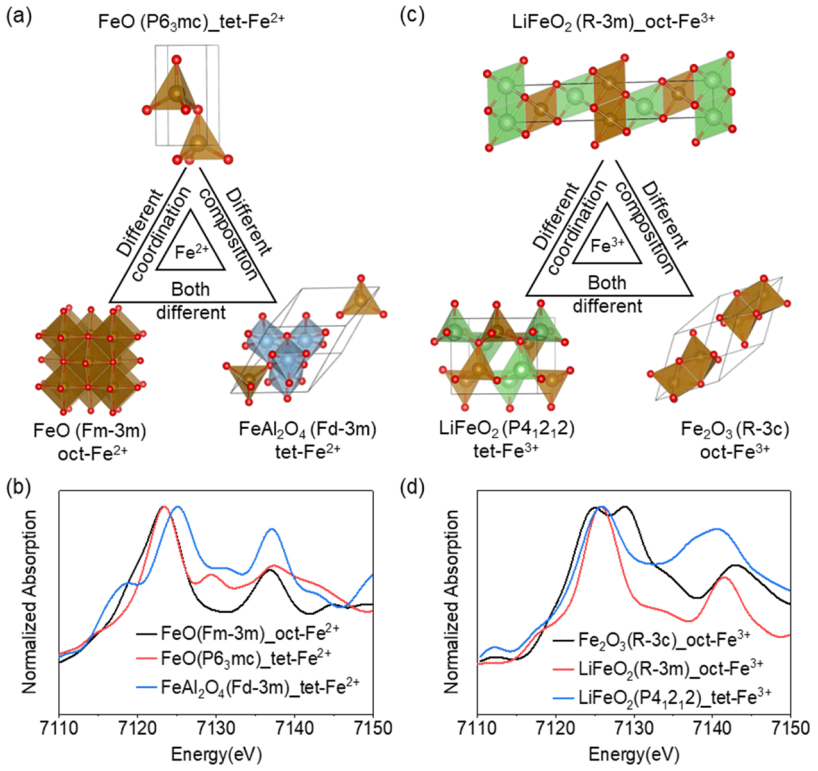

Figure 3. Comparing XANES spectra dependent on the local coordination and composition. Geometric structures and the simulated XANES spectra of Fe^{2+} (a and b) and Fe^{3+} (c and d) in oxides with different local coordinations, compositions, or both.

(main edge), a sharp main peak, which is usually referred to as a "white line", and a postedge. The energy range of the XANES spectrum is usually from the pre-edge to 50 eV, followed by the EXAFS region with an energy level of up to 1000 eV. XANES spectra contain characteristic electronic structures of the systems and will be the focus of the current work. The EXAFS spectra quantitatively provide local geometric parameters, including coordination numbers and bond lengths of a species with respect to surrounding atoms within 5 Å.[11] Thus, first-principles-based XANES simulations on various given structures provide a solid basis for accurately extracting both electronic structure and geometric structure information from the measured XAS.

As comparing XANES spectra of targeting catalysts with those of reference samples with well-defined structures and oxidation states is a standard approach in experiments to estimate their oxidation states, we start by comparing the simulated K-edge XANES spectra of FeO and α-Fe_2O_3 (Figure 1c,d), along with the measured spectra in our previous work.[4] In agreement with the measured XANES spectra, there are at least three major differences between FeO and Fe_2O_3 on the simulated ones, including large shifts on the main edges (e.g., ΔE_h = 2.4 eV at the half-maximum) and the main peaks (ΔE_p = 5.3 eV) and a more discernable pre-edge for Fe_2O_3 than that for FeO. These distinctions indicate that XANES is indeed efficient in distinguishing the oxidation state between Fe^{2+} in FeO and Fe^{3+} in Fe_2O_3. To further illustrate this point, in Figure 2, we have plotted the simulated Fe K-edge XANES spectra of two oxides with slightly more complex compositions, i.e., $FeAl_2O_4$ with Fe^{2+} and $LiFeO_2$ with Fe^{3+}, respectively. In agreement with FeO and Fe_2O_3, there are large shifts on the low-energy main edges (e.g., 2.8 eV at the 1/4 maximum) and a more discernable pre-edge for Fe^{3+} in $LiFeO_2$ than that for Fe^{2+} in $FeAl_2O_4$.[30] These results demonstrate again that XANES is a powerful tool to distinguish an element with different oxidation states.

While we focused on the oxidation state in the above comparisons, there are also apparent differences in XANES spectra for an element with the same oxidation state but different local coordinations, another parameter usually considered in comparing experimental spectra. For example, for the six-coordinated octahedral Fe^{3+} (oct-Fe^{3+}) in Fe_2O_3 and four-coordinated tetrahedral Fe^{3+} (tet-Fe^{3+}) in $LiFeO_2$ (Figure 2a), in addition to the difference in the intensity of the pre-edge, there are clear differences in the main edge in the energy range of 7120−7125 eV and in the postedge in the energy range above 7130 eV. For the six-coordinated octahedral Fe^{2+} (oct-Fe^{2+}) in FeO and the four-coordinated tetrahedra Fe^{2+} (tet-Fe^{2+}) in $FeAl_2O_4$ (Figure 2a), they have a completely different main edge, though corresponding pre-edges and the locations of the postedge peaks at high energies (i.e., ∼7143 eV) are essentially the same. These comparisons indicated that the oxidation state is not the dominant factor in the XANES line shape.

It is worth noting that, in addition to the local coordination, the above comparisons also involve a change of the nonlocal factors, e.g., crystal structure and composition. To better tell the nonlocal geometric effects from the local ones, we consider two more intermediates of tet-Fe^{2+} in FeO ($P6_3mc$) and oct-Fe^{3+} in $LiFeO_2$ ($R\bar{3}m$) and have oct-Fe^{2+} in FeO ($Fm\bar{3}m$) → tet-Fe^{2+} in FeO ($P6_3mc$) → tet-Fe^{2+} in $FeAl_2O_4$ and oct-Fe^{3+} in Fe_2O_3 → oct-Fe^{3+} in $LiFeO_2$ ($R\bar{3}m$) → tet-Fe^{3+} in $LiFeO_2$ ($P4_12_12$). In each of Fe^{2+} and/or Fe^{3+} series, there are differences in either composition or local coordination (oct vs tet) or both. In comparison with the large XANES differences between oct-Fe^{2+} in FeO ($Fm\bar{3}m$) and tet-Fe^{2+} in $FeAl_2O_4$ with

https://doi.org/10.1021/acs.jpcc.1c08461
J. Phys. Chem. C 2021, 125, 26229−26239

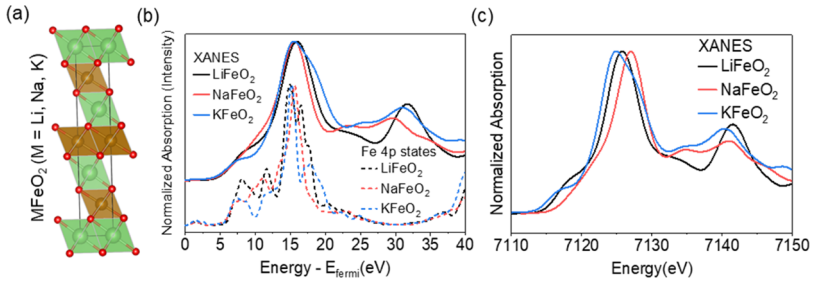

Figure 4. Comparing XANES spectra of compounds with the same crystal structure but different compositions. (a) Geometric structure of layered oxides $MFeO_2$ (M = Li, Na, and K) with space group $R\bar{3}m$. Their simulated XANES spectra and corresponding projected densities of Fe 4p states (density of states, DOS) at the energy scale referred to the Fermi level (b) and at the absolute energy scale (c).

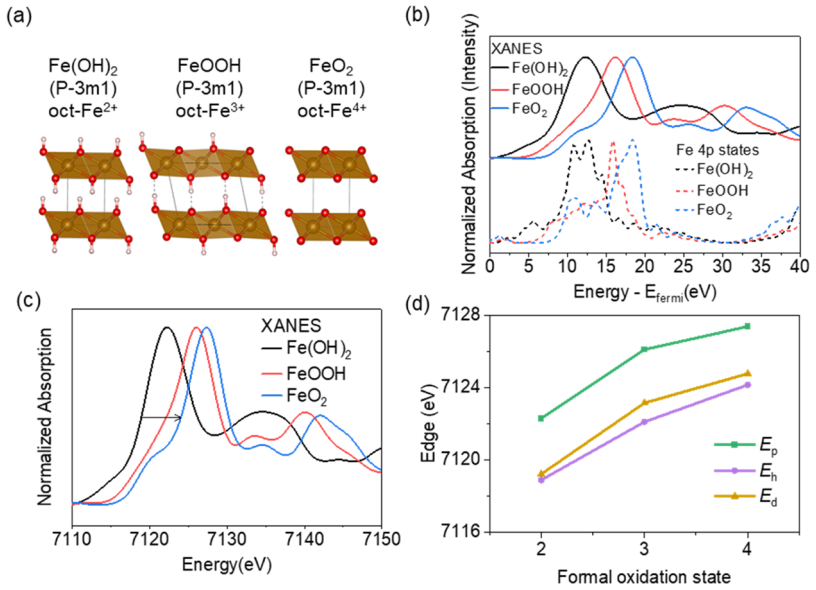

Figure 5. Comparing XANES spectra of compounds with the same crystal structure but different oxidation states. (a) Geometric structures of layered oxides $Fe(OH)_2$, FeOOHm and FeO_2 with space group $P\bar{3}m1$. Their simulated XANES spectra and corresponding projected densities of Fe 4p states (DOS) at the energy scale referred to the Fermi level (b) and at the absolute energy scale (c). (d) Three types of edge energies (see Figure 1 for their definition) as a function of the formal oxidation state.

different coordination symmetries and compositions (Figure 2b), the XANES differences between oct-Fe^{2+} in FeO ($Fm\bar{3}m$) and tet-Fe^{2+} in FeO ($P6_3mc$) with the same composition but different local coordination symmetries are much smaller (in Figure 3b). However, there are still large XANES differences between the intermediate tet-Fe^{2+} in FeO ($P6_3mc$) and tet-Fe^{2+} in $FeAl_2O_4$ on both the main edge and main peak, though they have the same local coordination, highlighting the larger influence of composition than local coordination on XANES line shapes. A similar scenario can be found for the intermediate oct-Fe^{3+} in $LiFeO_2$ ($R\bar{3}m$) (in Figure 3d). In comparison with the large XANES differences between tet-Fe^{3+} in $LiFeO_2$ ($P4_12_12$) and oct-Fe^{3+} in Fe_2O_3 with different coordination symmetries and compositions, the XANES differences between oct-Fe^{3+} in $LiFeO_2$ ($R\bar{3}m$) and tet-Fe^{3+} in $LiFeO_2$ ($P4_12_12$) with the same composition are smaller, though they have different local coordination symmetries. Again, the XANES differences between oct-Fe^{3+} in $LiFeO_2$ ($R\bar{3}m$) and oct-Fe^{3+} in Fe_2O_3 with different compositions remain large, despite their same local coordination symmetry, which confirms that composition is a more dominant factor than local coordination of XANES line shapes.

For compounds with the same composition, though the above results show a negligible shift on the main peaks (ΔE_p = 0), there are noticeable shifts on the main edges (ΔE_h). For example, the energy shift at the half maximum (ΔE_h) is 1.5 eV for oct-Fe^{2+} in FeO ($Fm\bar{3}m$) with respect to tet-Fe^{2+} in FeO ($P6_3mc$) and 1.0 eV for oct-Fe^{3+} in $LiFeO_2$ ($R\bar{3}m$) with respect to tet-Fe^{3+} in $LiFeO_2$ ($P4_12_12$) (in Figure 3). We note that, for the above compounds with the same composition, i.e., FeO and $LiFeO_2$, there are changes in both the local geometry and crystal structure. To separate the influence of these two parameters from composition, we simulate the XANES spectra of oct-Fe^{3+} in $MFeO_2$ (M = Li, Na, and K) with the same crystal structure and the same local environment in the first shell but different compositions in the second shell (Li, Na, and K), as shown in Figure 4b. The simulated XANES spectra of oct-Fe^{3+} indicates that, although there are small differences at the low-energy edge, spectra from these compounds (with respect to the Fermi level) overlap the main peaks and most of the main edges. When the core-level shifts have been considered, there are constant shifts of the main peak and most of the main edge (Figure 4c). Considering that the oxidation state and local coordination are not the dominant factors as being concluded above, the overlaps and constant shifts between the spectra of $MFeO_2$ suggest that the crystal structure even plays a more dominant role than composition in the line shape of XANES spectra. As extracting oxidation state

https://doi.org/10.1021/acs.jpcc.1c08461
J. Phys. Chem. C 2021, 125, 26229−26239

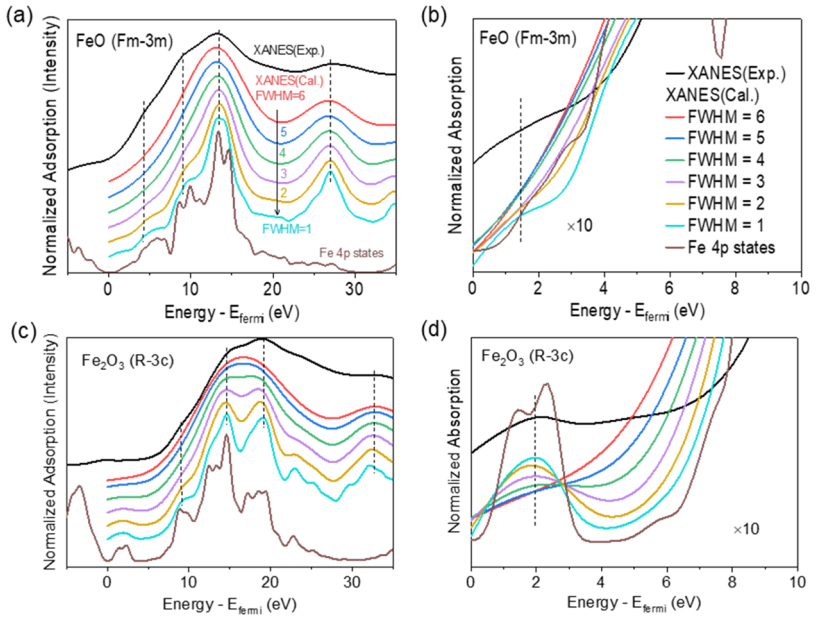

Figure 6. Influence of the broadening effect on the line shape of XANES spectra. (a) Comparison of peak positions between the measured (denoted Exp.) and simulated (denoted Cal.) XANES spectra of oxides (a) FeO ($Fm\bar{3}m$) and (b) Fe_2O_3 ($R\bar{3}c$) as a function of the broadening parameter FWHM from 1 to 6 eV as well as the projected density of Fe 4p states (DOS). (c and d) Ten-time magnification of (a) and (b), respectively. The dashed vertical lines indicate that the calculated main and shoulder peaks are all aligned at the measured ones.

through comparing the shifts of the main edge is the primary goal of XANES measurements, the crystal structure as a more dominant factor of the line shape implies that a reliable assignment of oxidation states can be achieved only by comparing to reference samples with the same or similar crystal structure or nonlocal structure for compounds without a well-defined crystal structure.

To verify the selection principle of the reference samples deduced above, we simulated Fe K-edge XANES spectra of $Fe(OH)_2$, FeOOH, and FeO_2 with the same $Fe(OH)_2$-type crystal structure but different Fe oxidation states (Figure 5). Consistent with the above conclusion, the simulated XANES spectra have very similar line shapes (Figure 5b,c), for which the main edges and main peaks shift to higher energy nearly in proportion to the increased oxidation state (Figure 5d). Such a shift is also consistent with Natoli's rule, i.e., the shifts are inversely proportional to the square of the Fe−O bond length (Figure S1 in the Supporting Information).[8,18] We note that when there is a difference in the crystal structure (e.g., FeO and Fe_2O_3), and especially when there is a change in the bond length but no change in the oxidation state ($MFeO_2$), this semiempirical rule becomes much less rigorous. These results emphasize the importance of clarifying the dominant factors of the XANES line shape in understanding the oxidation state and the bond length in response to the edge shift, i.e., the limitation of Natoli's rule. In addition, the dominant role of the crystal structure in the line shape of XANES spectra makes it possible to extract more structural information that is not directly available from the standard XAS measurement. Specifically, for the cases that the crystal structure or nonlocal structure is not available, it could be deduced partly through comparing the line shape of the measured XANES spectrum with that of well-defined reference samples or with computational XANES spectra of compounds with a variety of crystal structures. As EXAFS measurements can only provide local geometries of a catalyst, the possibility of extracting nonlocal structures from XANES measurements can significantly extend the power of XAS measurements.

Below, we will provide a fundamental understanding of dominant factors by unraveling the mechanistic origin in the evolution of XANES line shapes. Figure 6 shows the calculated DOSs of the unoccupied Fe 4p states of FeO and Fe_2O_3, along with the measured Fe K-edge XANES spectra (shifted to facilitate the comparison). K-edge is the excitation from Fe 1s orbitals to the unoccupied Fe 4p states. Thus, the shape of the Fe K-edge XANES spectrum is directly related to the corresponding DOS. However, there are much richer and sharper peaks from the calculated 4p states than from the measured XANES spectra. For example, there are at least three distinct regions of 4p states for both FeO and Fe_2O_3 from 5 to 20 eV with the fine structure in each region. However, there are only one main peak and two shoulders without any fine structure on measured XANES spectra for both FeO and Fe_2O_3. Also, there are apparent 4p states in the pre-edge region for the calculated DOS of both FeO and Fe_2O_3, probably induced through hybridization with the Fe 3d states. However, even for the enlarged XANES spectra, the pre-edge is nearly absent for FeO and merely discernable for Fe_2O_3.

The distinct differences between the measured XANES spectra and the calculated DOS are mainly caused by the energy resolution of X-rays used in the experiment and the core-hole lifetime of the element measured. We note there could be a contribution from the thermal effects, though the impact is not so important for crystals and solid compounds with strong chemical bonds as for aqueous ions with weak interactions (Figure S3).[62−64] Here, we use a parameter that is corresponding to the full width at half-maximum (FWHM) in the experiment to study the broadening effects caused by the above three factors by comparing the relative intensity of characteristic peaks. Figure 6 shows the simulated XANES spectra with FWHM from 1 to 6 eV. For FWHM = 1, the relative intensity of characteristic peaks is high and resembles

https://doi.org/10.1021/acs.jpcc.1c08461
J. Phys. Chem. C 2021, 125, 26229−26239

those from DOS but decreases with increasing FWHM. A reasonable agreement between the experiment and modeling is achieved on both pre-edge regions and main edge regions with FWHM = 3 eV. A further increase of the FWHM leads to the disappearance of some characteristic peaks, especially the peaks in the pre-edge region. Thus, we used FWHM = 3 eV in our XANES modeling to mimic the broadening effect caused by X-ray energy resolution, the core-hole lifetime, and the thermal effects.

The above analyses of the broadening effect and the comparison with the corresponding DOS could help clarify the origin of the distinct XANES fingerprint of an element in each individual compound. For example, for oct-Fe^{3+} in Fe_2O_3 versus oct-Fe^{2+} in FeO ($Fm\bar{3}m$) with the same local coordination but different oxidation states, there are clear shifts of the main Fe 4p states toward higher energy with increasing oxidation state, accompanied by a change of the intensity (Figure 7a). Through simulated XANES with

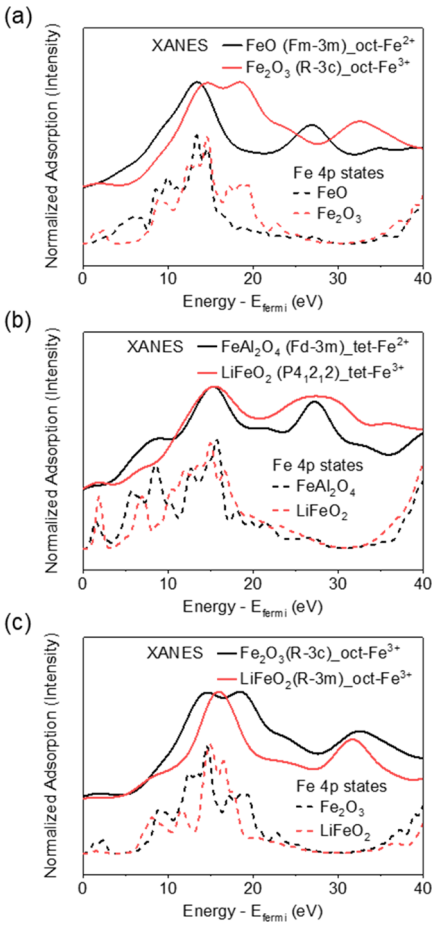

Figure 7. Correlation of XANES features with Fe 4p DOS. Simulated XANES spectra and corresponding projected densities of Fe 4p state plots of Fe^{2+} and Fe^{3+} with the same local coordination but different oxidation states (a, b) or different compositions and crystal structures (c).

increasing FWHM, it is evidenced that the blue shift of DOS is the origin of the overall shift of the main edge and the main peak of Fe_2O_3 versus that of FeO. The above simple shifts of DOS in response to a change in the oxidation state do not hold true for tet-Fe^{3+} in $LiFeO_2$ ($P4_12_12$) versus tet-Fe^{2+} in $FeAl_2O_4$, which have again the same local coordination but different oxidation states (Figure 7b). Their shifts of Fe 4p states are more complex than that of Fe_2O_3 versus FeO ($Fm\bar{3}m$). Specifically, while there are clear shifts toward higher energy for the first two main Fe 4p states at the low energy (5−10 eV), there is little shift for the Fe 4p states at the high energy (10−15 eV). As a consequence, instead of a simultaneous shift of both the main edge and the main peak in XANES spectra as the case of oct-Fe^{3+} in Fe_2O_3 versus oct-Fe^{2+} in FeO ($Fm\bar{3}m$), there is only a shift of the low-energy main edge in XANES spectra, which is corresponding to the first two peaks of the Fe 4p states (Figure 7b). These nonsimultaneous shifts are the fundamental reason that the oxidation state is not the dominant factor of the XANES line shapes.

For oct-Fe^{3+} in Fe_2O_3 versus oct-Fe^{3+} in $LiFeO_2$ ($R\bar{3}m$), which have the same coordination and oxidation state, instead of nonsimultaneous shifts, the differences are mainly in the splitting of the major Fe 4p states in the range of 12−20 eV with respect to the Fermi level (Figure 7c). For oct-Fe^{3+} in $LiFeO_2$ ($R\bar{3}m$), these major Fe 4p states are concentrated at around 15 eV, while for oct-Fe^{3+} in Fe_2O_3, the corresponding 4p states split into a width that is about twice that of oct-Fe^{3+} in Fe_2O_3. As a consequence, for the simulated XANES spectra, there is not only a two-time difference in the width of the main peaks but also a 2.2 eV shift in the main edge, though there is no change in both the oxidation state and the local coordination. This difference in the splitting and width of the major Fe 4p state is the origin why both local coordination and oxidation state are not the dominant factors of the XANES line shape.

As the crystal structure is the dominant factor of the XANES line shapes, the above comparisons imply a similarity in major Fe 4p states for those with the same or similar nonlocal structures. To verify this deduction, we plotted the DOS of $MFeO_2$ (M = Li, Na, and K) with the same crystal structure ($R\bar{3}m$) (Figure 4a). Indeed, although there are still differences in the DOS in the energy range of 10−15 eV with respect to the Fermi level, the major 4p states from 15 to 20 eV have strong similarities, including the intensity, width, and energy range. Consequently, the simulated XANES spectra overlap the main peaks and most of the main edges, which shift simultaneously when the core-level shifts have been taken into account (Figure 4c). This is also the case for $Fe(OH)_2$, FeOOH, and FeO_2, with the $Fe(OH)_2$-type crystal structure, i.e., they have similar complexity in the major 4p states (Figure 5b). Although there are differences in details, the broadening effects make them a simultaneous shift in the main peaks and the main edges of the simulated XANES spectra. Therefore, although rooted in DOS, XANES spectra with broadening effects can shed light on both the oxidation state and nonlocal geometry that DOS with excessive details cannot.

Below, we discuss the dominant factors that determine the discernibility of the pre-edge. In Figure 6c,d, the disappearance of the pre-edge feature with increasing FWHM indicates that the absence of pre-edge in the experiment might not be because of the absence of Fe 4p states around the common pre-edge energy region but the broadening effect caused by X-ray energy resolution, the core-hole lifetime, and the thermal effects. Thus, for the same or similar broadening effect, the presence or absence of pre-edges in experiments could depend on two factors: the intensity of Fe 4p states around the pre-edge region and their energy difference from Fe 4p states that contribute to the main edge. The former determines the intrinsic intensify of the pre-edge, while the latter determines

https://doi.org/10.1021/acs.jpcc.1c08461
J. Phys. Chem. C 2021, 125, 26229−26239

whether the pre-edge could be distinguished from the main edge.

For example, for oct-Fe^{2+} in FeO ($Fm\bar{3}m$), the intensities of the Fe 4p states around the pre-edge are extremely low and their energy difference from Fe 4p states that contribute to the main energy is essentially 0 eV (Figure 8a). Thus, the simulated pre-edge in the XANES spectrum is nearly undiscernible even if FWHM is relatively small, e.g., FWHM = 1 eV (Figure 6a). As the FWHM in the experiment is around 3 eV, it implies that pre-edge in the measured XANES spectrum is basically absent, which is exactly the case (Figure 1d). For tet-Fe^{2+} in $FeAl_2O_4$, it has a much higher intensity for the Fe 4p states around the pre-edge and a much larger energy difference between the corresponding 4p states and the Fe 4p states of the main edge (i.e., dE = ∼3.3 eV, see Figure 8a). Therefore, the simulated pre-edge of tet-Fe^{2+} in $FeAl_2O_4$ is much more discernable than that of oct-Fe^{2+} in FeO ($Fm\bar{3}m$) and disappears at a much larger FWHM (>3 eV for $FeAl_2O_4$ versus >1 eV for FeO). Thus, we can predict that the measured pre-edge of $FeAl_2O_4$ is more discernable than that of FeO. Such a difference is exactly observed in previous experiments.[30]

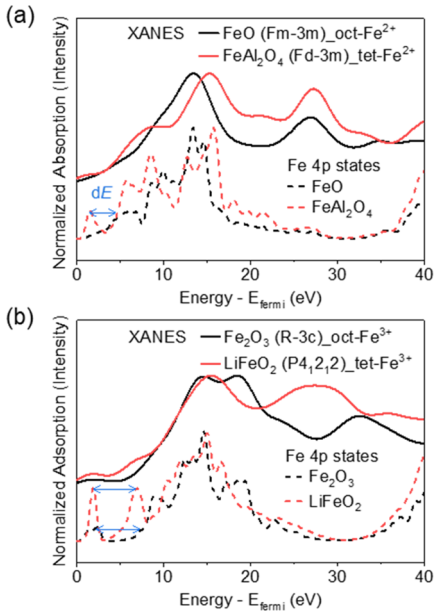

Figure 8. Correlation of the pre-edge with Fe 4p states. Simulated XANES spectra and corresponding projected densities of Fe 4p state plots of Fe^{2+} (a) and Fe^{3+} (b) with different local coordinations.

For Fe^{3+} in Fe_2O_3 and $LiFeO_2$ ($P4_12_12$), even though there is not always an increase in the intensity of 4p states around the pre-edge in comparison to that of Fe^{2+} in $FeAl_2O_4$, the energy difference between the Fe 4p states around the main edge and the corresponding 4p states of the main edge increases from ∼3.3 to ∼5.2 and ∼4.8 eV, respectively (Figure 8b). As these energy differences are about 2 eV larger than the FWHM in the experiment (∼3 eV), consequently, the pre-edges of Fe^{3+} in both Fe_2O_3 and $LiFeO_2$ are clearly discernable at FWHM = 3 eV. These results suggest that these pre-edges are present in the measured XANES spectrum, which are indeed the cases in previous experiments.[30] As it generally increases with the increased Fe oxidation state for the energy difference between the Fe 4p states around the pre-edge and the corresponding 4p states of the main edge (see Figure 5), it suggests the presence of pre-edges for Fe with 3+ or higher oxidation states. Such general phenomena have been widely observed in experiments.[30,65−67] It is worth noting that their discernibility also depends on the intensity of Fe 4p states induced by hybridization with Fe 3d states around the pre-edge. As there is no clear relationship between the intensity of these Fe 4p states and the corresponding oxidation states, XANES modeling provides a straightforward way to predict and interpret the complex pre-edge features. Also, as the pre-edge is very sensitive to these detailed electronic structures, modeling using appropriate crystal structures and electronic structures (e.g., spin states, see Figure S2 in the Supporting Information) is crucial for a rigorous comparison with experimental results.

CONCLUSIONS

In the present work, using Fe K-edge XANES spectra as an example, we showed that XANES spectra are sensitive to an ensemble of multiple parameters, including the oxidation state, local coordination chemical composition, and nonlocal structure (e.g., crystal structure). We demonstrated that first-principles-based modeling can shed light not only on the challenging assignment and on the interpretation of complex XANES spectra but also extend the power of XANES measurements. More specifically, we found that nonlocal structure, which is inaccessible in XAS measurements, is a more dominant factor of the XANES line shapes than either composition and factors (i.e., local geometry or the apparent oxidation state) that are usually extracted from XAS measurements. For compounds with the same or similar crystal structures (e.g., layered oxides $MFeO_2$ (M = Li, Na, K) and FeO_2H_x (x = 2, 1, 0)), both the main edges and postedges are alike and shifting simultaneously in response to a change in the chemical environment. Such a correlation between the line shape and the nonlocal structure not only provides practical principles for the reliable assignment of spectra of oxidation states for materials with known structures and for understanding the limitation of semiempirical rules but also makes it possible to extract structural information that is not directly accessible in XAS measurements. For the pre-edge, we found that its discernibility is dominated by the intensity of Fe 4p states induced by hybridization with Fe 3d states around the pre-edge and their energy difference from Fe 4p states that contribute to the main edge. As the latter usually increases with increasing oxidation state, it suggests a more discernable pre-edge for Fe with a higher oxidation state, as is generally observed in experiments. In summary, the current work not only provides insights into understanding and assigning the oxidation state of measured spectra but also unravels critical nonlocal structures hidden in the experimental measurement.

ASSOCIATED CONTENT

Supporting Information

The Supporting Information is available free of charge at https://pubs.acs.org/doi/10.1021/acs.jpcc.1c08461.

Geometric structure and magnetic moment information of Fe-based oxides, relationship between edge positions and bond lengths, and magnetic configuration effect and thermal effect on the simulated XANES spectra (PDF)

Geometric structures of Fe-based oxides (ZIP)

https://doi.org/10.1021/acs.jpcc.1c08461
J. Phys. Chem. C 2021, 125, 26229−26239

AUTHOR INFORMATION

Corresponding Authors

Zhenhua Zeng − *Davidson School of Chemical Engineering, Purdue University, West Lafayette, Indiana 47907, United States*; Email: zeng46@purdue.edu

Wei-Xue Li − *Department of Chemical Physics, School of Chemistry and Materials Science and Hefei National Laboratory for Physical Sciences at the Microscale, University of Science and Technology of China, Hefei 230026, China*; orcid.org/0000-0002-5043-3088; Email: wxli70@ustc.edu.cn

Author

Jing Zhu − *Department of Chemical Physics, School of Chemistry and Materials Science, University of Science and Technology of China, Hefei 230026, China*

Complete contact information is available at: https://pubs.acs.org/10.1021/acs.jpcc.1c08461

Notes

The authors declare no competing financial interest.

ACKNOWLEDGMENTS

This work was supported by the National Key R&D Program of China (2018YFA0208603), the National Natural Science Foundation of China (91945302), the Chinese Academy of Sciences (QYZDJ-SSW-SLH054), and K.C. Wong Education (GJTD-2020-15). The authors also gratefully thank the Supercomputing Center of the University of Science and Technology of China. The work at Purdue was supported by the Office of Science, Office of Basic Energy Sciences, Chemical, Biological, and Geosciences Division under DE-SC0010379 and an ECS Toyota Young Investigator Fellowship.

REFERENCES

(1) Hüfner, S. *Photoelectron Spectroscopy: Principles and Applications*, 3rd ed.; Springer: Berlin, 2003; p 677.

(2) Bokhoven, J. A. V.; Lamberti, C. *X-Ray Absorption and X-Ray Emission Spectroscopy: Theory and Applications*; John Wiley & Sons, Ltd, 2016.

(3) Evans, J. *X-Ray Absorption Spectroscopy for the Chemical and Materials Sciences*; John Wiley & Sons Ltd, 2018.

(4) Dionigi, F.; Zeng, Z.; Sinev, I.; Merzdorf, T.; Deshpande, S.; Lopez, M. B.; Kunze, S.; Zegkinoglou, I.; Sarodnik, H.; Fan, D.; et al. In-Situ Structure and Catalytic Mechanism of NiFe and CoFe Layered Double Hydroxides During Oxygen Evolution. *Nat. Commun.* **2020**, *11*, No. 2522.

(5) Zeng, Z.-H.; Ma, X.-F.; Ding, W.-C.; Li, W.-X. First-Principles Calculation of Surface Core-Level Shift in Surface Chemical Processes. *Sci. China: Chem.* **2010**, *53*, 402−410.

(6) Biasin, E.; Nascimento, D. R.; Poulter, B. I.; Abraham, B.; Kunnus, K.; Garcia-Esparza, A. T.; Nowak, S. H.; Kroll, T.; Schoenlein, R. W.; Alonso-Mori, R.; et al. Revealing the Bonding of Solvated Ru Complexes with Valence-to-Core Resonant Inelastic X-Ray Scattering. *Chem. Sci.* **2021**, *12*, 3713−3725.

(7) Nascimento, D. R.; Biasin, E.; Poulter, B. I.; Khalil, M.; Sokaras, D.; Govind, N. Resonant Inelastic X-Ray Scattering Calculations of Transition Metal Complexes within a Simplified Time-Dependent Density Functional Theory Framework. *J. Chem. Theory Comput.* **2021**, *17*, 3031−3038.

(8) Timoshenko, J.; Roldan Cuenya, B. In Situ/Operando Electrocatalyst Characterization by X-Ray Absorption Spectroscopy. *Chem. Rev.* **2021**, *121*, 882−961.

(9) Timoshenko, J.; Frenkel, A. I. "Inverting" X-Ray Absorption Spectra of Catalysts by Machine Learning in Search for Activity Descriptors. *ACS Catal.* **2019**, *9*, 10192−10211.

(10) Li, J.; Gong, J. Operando Characterization Techniques for Electrocatalysis. *Energy Environ. Sci.* **2020**, *13*, 3748−3779.

(11) Wang, M.; Árnadóttir, L.; Xu, Z. J.; Feng, Z. In Situ X-Ray Absorption Spectroscopy Studies of Nanoscale Electrocatalysts. *Nano-Micro Lett.* **2019**, *11*, No. 47.

(12) Deng, J.; Zhang, Q.; Lv, X.; Zhang, D.; Xu, H.; Ma, D.; Zhong, J. Understanding Photoelectrochemical Water Oxidation with X-Ray Absorption Spectroscopy. *ACS Energy Lett.* **2020**, *5*, 975−993.

(13) Suzuki, Y.; Hino, H.; Kotsugi, M.; Ono, K. Automated Estimation of Materials Parameter from X-Ray Absorption and Electron Energy-Loss Spectra with Similarity Measures. *npj Comput. Mater.* **2019**, *5*, No. 39.

(14) Holden, W. M.; Jahrman, E. P.; Govind, N.; Seidler, G. T. Probing Sulfur Chemical and Electronic Structure with Experimental Observation and Quantitative Theoretical Prediction of Kα and Valence-to-Core Kβ X-Ray Emission Spectroscopy. *J. Phys. Chem. A* **2020**, *124*, 5415−5434.

(15) Jahrman, E. P.; Holden, W. M.; Govind, N.; Kas, J. J.; Rana, J.; Piper, L. F. J.; Siu, C.; Whittingham, M. S.; Fister, T. T.; Seidler, G. T. Valence-to-Core X-Ray Emission Spectroscopy of Vanadium Oxide and Lithiated Vanadyl Phosphate Materials. *J. Mater. Chem. A* **2020**, *8*, 16332−16344.

(16) Li, J.; Güttinger, R.; Moré, R.; Song, F.; Wan, W.; Patzke, G. R. Frontiers of Water Oxidation: The Quest for True Catalysts. *Chem. Soc. Rev.* **2017**, *46*, 6124−6147.

(17) Wong, J.; Lytle, F. W.; Messmer, R. P.; Maylotte, D. H. K-Edge Absorption Spectra of Selected Vanadium Compounds. *Phys. Rev. B* **1984**, *30*, 5596−5610.

(18) Glatzel, P.; Smolentsev, G.; Bunker, G. The Electronic Structure in 3d Transition Metal Complexes: Can We Measure Oxidation States? *J. Phys.: Conf. Ser.* **2009**, *190*, No. 012046.

(19) Bianconi, A.; Fritsch, E.; Calas, G.; Petiau, J. X-Ray-Absorption near-Edge Structure of 3d Transition Elements in Tetrahedral Coordination: The Effect of Bond-Length Variation. *Phys. Rev. B* **1985**, *32*, 4292−4295.

(20) Zeng, Z.; Chang, K.-C.; Kubal, J.; Markovic, N. M.; Greeley, J. Stabilization of Ultrathin (Hydroxy)Oxide Films on Transition Metal Substrates for Electrochemical Energy Conversion. *Nat. Energy* **2017**, *2*, No. 17070.

(21) Chung, D. Y.; Lopes, P. P.; Martins, P. F.; He, H.; Kawaguchi, T.; Zapol, P.; You, H.; Tripkovic, D.; Strmcnik, D.; Zhu, Y.; et al. Dynamic Stability of Active Sites in Hydr(Oxy)Oxides for the Oxygen Evolution Reaction. *Nat. Energy* **2020**, *5*, 222−230.

(22) Cesar, L. G.; Yang, C.; Lu, Z.; Ren, Y.; Zhang, G.; Miller, J. T. Identification of a Pt_3Co Surface Intermetallic Alloy in Pt−Co Propane Dehydrogenation Catalysts. *ACS Catal.* **2019**, *9*, 5231−5244.

(23) Subbaraman, R.; Tripkovic, D.; Chang, K.-C.; Strmcnik, D.; Paulikas, A. P.; Hirunsit, P.; Chan, M.; Greeley, J.; Stamenkovic, V.; Markovic, N. M. Trends in Activity for the Water Electrolyser Reactions on 3d M(Ni,Co,Fe,Mn) Hydr(Oxy)Oxide Catalysts. *Nat. Mater.* **2012**, *11*, 550−557.

(24) Jia, Q.; Ramaswamy, N.; Hafiz, H.; Tylus, U.; Strickland, K.; Wu, G.; Barbiellini, B.; Bansil, A.; Holby, E. F.; Zelenay, P.; et al. Experimental Observation of Redox-Induced Fe−N Switching Behavior as a Determinant Role for Oxygen Reduction Activity. *ACS Nano* **2015**, *9*, 12496−12505.

(25) Jiao, L.; Wan, G.; Zhang, R.; Zhou, H.; Yu, S.-H.; Jiang, H.-L. From Metal−Organic Frameworks to Single-Atom Fe Implanted N-Doped Porous Carbons: Efficient Oxygen Reduction in Both Alkaline and Acidic Media. *Angew. Chem., Int. Ed.* **2018**, *57*, 8525−8529.

(26) Kuai, C.; Xu, Z.; Xi, C.; Hu, A.; Yang, Z.; Zhang, Y.; Sun, C.-J.; Li, L.; Sokaras, D.; Dong, C.; et al. Phase Segregation Reversibility in Mixed-Metal Hydroxide Water Oxidation Catalysts. *Nat. Catal.* **2020**, *3*, 743−753.

(27) Gu, J.; Hsu, C.-S.; Bai, L.; Chen, H. M.; Hu, X. Atomically Dispersed Fe^{3+} Sites Catalyze Efficient CO_2 Electroreduction to Co. *Science* **2019**, *364*, 1091−1094.
(28) Cao, L.; Liu, W.; Luo, Q.; Yin, R.; Wang, B.; Weissenrieder, J.; Soldemo, M.; Yan, H.; Lin, Y.; Sun, Z.; et al. Atomically Dispersed Iron Hydroxide Anchored on Pt for Preferential Oxidation of CO in H_2. *Nature* **2019**, *565*, 631−635.
(29) Kuai, C.; Zhang, Y.; Wu, D.; Sokaras, D.; Mu, L.; Spence, S.; Nordlund, D.; Lin, F.; Du, X.-W. Fully Oxidized Ni−Fe Layered Double Hydroxide with 100% Exposed Active Sites for Catalyzing Oxygen Evolution Reaction. *ACS Catal.* **2019**, *9*, 6027−6032.
(30) Wilke, M.; Farges, F.; Petit, P.-E.; Brown, G. E., Jr.; Martin, F. Oxidation State and Coordination of Fe in Minerals: An Fe K-Xanes Spectroscopic Study. *Am. Mineral.* **2001**, *86*, 714−730.
(31) Piquer, C.; Laguna-Marco, M.; Roca, A. G.; Boada, R.; Guglieri, C.; Chaboy, J. Fe K-Edge X-Ray Absorption Spectroscopy Study of Nanosized Nominal Magnetite. *J. Phys. Chem. C* **2014**, *118*, 1332−1346.
(32) Mottram, L. M.; Cafferkey, S.; Mason, A. R.; Oulton, T.; Kuan Sun, S.; Bailey, D. J.; Stennett, M. C.; Hyatt, N. C. A Feasibility Investigation of Speciation by Fe K-Edge Xanes Using a Laboratory X-Ray Absorption Spectrometer. *J. Geosci.* **2020**, *65*, 27−35.
(33) Westre, T. E.; Kennepohl, P.; DeWitt, J. G.; Hedman, B.; Hodgson, K. O.; Solomon, E. I. A Multiplet Analysis of Fe K-Edge 1s → 3d Pre-Edge Features of Iron Complexes. *J. Am. Chem. Soc.* **1997**, *119*, 6297−6314.
(34) Kasper, J. M.; Stetina, T. F.; Jenkins, A. J.; Li, X. Ab Initio Methods for L-Edge X-Ray Absorption Spectroscopy. *Chem. Phys. Rev.* **2020**, *1*, No. 011304.
(35) Sergentu, D.-C.; Duignan, T. J.; Autschbach, J. Ab Initio Study of Covalency in the Ground Versus Core-Excited States and X-Ray Absorption Spectra of Actinide Complexes. *J. Phys. Chem. Lett.* **2018**, *9*, 5583−5591.
(36) Joly, Y.; Bunău, O.; Lorenzo, J. E.; Galéra, R. M.; Grenier, S.; Thompson, B. Self-Consistency, Spin-Orbit and Other Advances in the FDMNES Code to Simulate Xanes and Rxd Experiments. *J. Phys.: Conf. Ser.* **2009**, *190*, No. 012007.
(37) Benfatto, M.; Della Longa, S.; Pace, E.; Chillemi, G.; Padrin, C.; Natoli, C. R.; Sanna, N. MXAN: A New Program for Ab-Initio Structural Quantitative Analysis of XANES Experiments. *Comput. Phys. Commun.* **2021**, *265*, No. 107992.
(38) Vinson, J.; Rehr, J. J.; Kas, J. J.; Shirley, E. L. Bethe-Salpeter Equation Calculations of Core Excitation Spectra. *Phys. Rev. B* **2011**, *83*, No. 115106.
(39) Rehr, J. J.; Kas, J. J.; Vila, F. D.; Prange, M. P.; Jorissen, K. Parameter-Free Calculations of X-Ray Spectra with FEFF9. *Phys. Chem. Chem. Phys.* **2010**, *12*, 5503−5513.
(40) Valiev, M.; Bylaska, E. J.; Govind, N.; Kowalski, K.; Straatsma, T. P.; Van Dam, H. J. J.; Wang, D.; Nieplocha, J.; Apra, E.; Windus, T. L.; et al. Nwchem: A Comprehensive and Scalable Open-Source Solution for Large Scale Molecular Simulations. *Comput. Phys. Commun.* **2010**, *181*, 1477−1489.
(41) Zheng, C.; Mathew, K.; Chen, C.; Chen, Y.; Tang, H.; Dozier, A.; Kas, J. J.; Vila, F. D.; Rehr, J. J.; Piper, L. F. J.; et al. Automated Generation and Ensemble-Learned Matching of X-Ray Absorption Spectra. *npj Comput. Mater.* **2018**, *4*, No. 12.
(42) Mathew, K.; Zheng, C.; Winston, D.; Chen, C.; Dozier, A.; Rehr, J. J.; Ong, S. P.; Persson, K. A. High-Throughput Computational X-Ray Absorption Spectroscopy. *Sci. Data* **2018**, *5*, No. 180151.
(43) Van Bokhoven, J. Recent Developments in X-Ray Absorption Spectroscopy. *Phys. Chem. Chem. Phys.* **2010**, *12*, No. 5502.
(44) Ankudinov, A. L.; Ravel, B.; Rehr, J. J.; Conradson, S. D. Real-Space Multiple-Scattering Calculation and Interpretation of X-Ray-Absorption near-Edge Structure. *Phys. Rev. B* **1998**, *58*, 7565−7576.
(45) Jain, A.; Ong, S. P.; Hautier, G.; Chen, W.; Richards, W. D.; Dacek, S.; Cholia, S.; Gunter, D.; Skinner, D.; Ceder, G.; et al. Commentary: The Materials Project: A Materials Genome Approach to Accelerating Materials Innovation. *APL Mater.* **2013**, *1*, No. 011002.
(46) Li, L.; Lee, E.; Freeland, J. W.; Fister, T. T.; Thackeray, M. M.; Chan, M. K. Y. Identifying the Chemical Origin of Oxygen Redox Activity in Li-Rich Anti-Fluorite Lithium Iron Oxide by Experimental and Theoretical X-Ray Absorption Spectroscopy. *J. Phys. Chem. Lett.* **2019**, *10*, 806−812.
(47) Fu, Q.; Li, W.-X.; Yao, Y.; Liu, H.; Su, H.-Y.; Ma, D.; Gu, X.-K.; Chen, L.; Wang, Z.; Zhang, H.; et al. Interface-Confined Ferrous Centers for Catalytic Oxidation. *Science* **2010**, *328*, 1141−1144.
(48) Wu, G.; More, K. L.; Johnston, C. M.; Zelenay, P. High-Performance Electrocatalysts for Oxygen Reduction Derived from Polyaniline, Iron, and Cobalt. *Science* **2011**, *332*, 443−447.
(49) Trotochaud, L.; Young, S. L.; Ranney, J. K.; Boettcher, S. W. Nickel−Iron Oxyhydroxide Oxygen-Evolution Electrocatalysts: The Role of Intentional and Incidental Iron Incorporation. *J. Am. Chem. Soc.* **2014**, *136*, 6744−6753.
(50) Ljungberg, M.; Mortensen, J. J.; Pettersson, L. An Implementation of Core Level Spectroscopies in a Real Space Projector Augmented Wave Density Functional Theory Code. *J. Electron Spectrosc. Relat. Phenom.* **2011**, *184*, 427−439.
(51) Enkovaara, J.; Rostgaard, C.; Mortensen, J. J.; Chen, J.; Dułak, M.; Ferrighi, L.; Gavnholt, J.; Glinsvad, C.; Haikola, V.; Hansen, H. Electronic Structure Calculations with Gpaw: A Real-Space Implementation of the Projector Augmented-Wave Method. *J. Phys.: Condens. Matter* **2010**, *22*, No. 253202.
(52) Mortensen, J. J.; Hansen, L. B.; Jacobsen, K. W. Real-Space Grid Implementation of the Projector Augmented Wave Method. *Phys. Rev. B* **2005**, *71*, No. 035109.
(53) Hjorth Larsen, A.; Jørgen Mortensen, J.; Blomqvist, J.; Castelli, I. E.; Christensen, R.; Dułak, M.; Friis, J.; Groves, M. N.; Hammer, B.; Hargus, C.; et al. The Atomic Simulation Environment—a Python Library for Working with Atoms. *J. Phys.: Condens. Matter* **2017**, *29*, No. 273002.
(54) Perdew, J. P.; Burke, K.; Ernzerhof, M. Generalized Gradient Approximation Made Simple. *Phys. Rev. Lett.* **1996**, *77*, No. 3865.
(55) Dudarev, S.; Botton, G.; Savrasov, S.; Humphreys, C.; Sutton, A. Electron-Energy-Loss Spectra and the Structural Stability of Nickel Oxide: An LSDA+ U Study. *Phys. Rev. B* **1998**, *57*, No. 1505.
(56) de Lima, G. F.; Duarte, H. l. A.; Pettersson, L. G. X-Ray Absorption near-Edge Spectroscopy Calculations on Pristine and Modified Chalcopyrite Surfaces. *J. Phys. Chem. C* **2018**, *122*, 20200−20209.
(57) Bajdich, M.; García-Mota, M.; Vojvodic, A.; Nørskov, J. K.; Bell, A. T. Theoretical Investigation of the Activity of Cobalt Oxides for the Electrochemical Oxidation of Water. *J. Am. Chem. Soc.* **2013**, *135*, 13521−13530.
(58) Lutfalla, S.; Shapovalov, V.; Bell, A. T. Calibration of the DFT/GGA+U Method for Determination of Reduction Energies for Transition and Rare Earth Metal Oxides of Ti, V, Mo, and Ce. *J. Chem. Theory Comput.* **2011**, *7*, 2218−2223.
(59) Klimeš, J.; Bowler, D. R.; Michaelides, A. Van der Waals Density Functionals Applied to Solids. *Phys. Rev. B* **2011**, *83*, No. 195131.
(60) Nilsson, A.; Pettersson, L. G. M. Chemical Bonding on Surfaces Probed by X-Ray Emission Spectroscopy and Density Functional Theory. *Surf. Sci. Rep.* **2004**, *55*, 49−167.
(61) Triguero, L.; Pettersson, L.; Ågren, H. Calculations of near-Edge X-Ray-Absorption Spectra of Gas-Phase and Chemisorbed Molecules by Means of Density-Functional and Transition-Potential Theory. *Phys. Rev. B* **1998**, *58*, No. 8097.
(62) Müller, P.; Karhan, K.; Krack, M.; Gerstmann, U.; Schmidt, W. G.; Bauer, M.; Kühne, T. D. Impact of Finite-Temperature and Condensed-Phase Effects on Theoretical X-Ray Absorption Spectra of Transition Metal Complexes. *J. Comput. Chem.* **2019**, *40*, 712−716.
(63) Campbell, L.; Rehr, J. J.; Schenter, G. K.; McCarthy, M. I.; Dixon, D. XAFS Debye-Waller Factors in Aqueous Cr+3 from Molecular Dynamics. *J. Synchrotron Radiat.* **1999**, *6*, 310−312.
(64) Ross, M.; Andersen, A.; Fox, Z. W.; Zhang, Y.; Hong, K.; Lee, J. H.; Cordones, A.; March, A. M.; Doumy, G.; Southworth, S. H.; et al. Comprehensive Experimental and Computational Spectroscopic

Study of Hexacyanoferrate Complexes in Water: From Infrared to X-Ray Wavelengths. *J. Phys. Chem. B* **2018**, *122*, 5075−5086.
(65) Okudera, H.; Yoshiasa, A.; Murai, K.-i.; Okube, M.; Takeda, T.; Kikkawa, S. Local Structure of Magnetite and Maghemite and Chemical Shift in Fe K-Edge Xanes. *J. Mineral. Petrol. Sci.* **2012**, *107*, 127−132.
(66) Deb, A.; Ralph, J. M.; Cairns, E. J.; Bergmann, U. Characterization of $La_{0.8}Sr_{0.2}FeO_{3-\delta}$ and $La_{0.7}Sr_{0.2}FeO_{3-\delta}$ as a Function of Temperature by X-Ray Absorption Spectroscopy. *Phys. Rev. B* **2006**, *73*, No. 115114.
(67) Berry, J. F.; Bill, E.; Bothe, E.; George, S. D.; Mienert, B.; Neese, F.; Wieghardt, K. An Octahedral Coordination Complex of Iron (Vi). *Science* **2006**, *312*, 1937−1941.

https://doi.org/10.1021/acs.jpcc.1c08461
J. Phys. Chem. C 2021, 125, 26229−26239